



# A numerical investigation on determining the failure strength of a powder compact in unconfined compression testing by considering the compressible character of the specimen



Hyunho Shin <sup>a,\*</sup>, Jong-Bong Kim <sup>b,\*</sup>

<sup>a</sup> Department of Materials Engineering, Gangneung-Wonju National University, 7 Jugheon-gil, Gangneung, Gangwon-do 210-702, Republic of Korea

<sup>b</sup> Department of Mechanical and Automotive Engineering, Seoul National University of Science and Technology, 232 Gongneung-ro, Nowon-gu, Seoul 139-743, Republic of Korea

## ARTICLE INFO

### Article history:

Received 30 November 2014

Received in revised form 5 January 2015

Accepted 25 February 2015

Available online 4 March 2015

### Keywords:

Failure strength

Unconfined compression test

Compressibility

Powder compact

## ABSTRACT

The effect of the compressible character of a powder compact on the determined failure strength in unconfined compression testing is investigated numerically. The modified Drucker–Prager cap constitutive model (an elastic–plastic–work hardening model) is employed for a spray-dried Al<sub>2</sub>O<sub>3</sub> powder compact. When the failure strength is obtained from the current cross sectional area determined solely by the axial strain based on the assumption of incompressibility of the specimen, it underestimates the failure strength of the compressible specimen significantly. The degree of underestimation is magnified if the powder compact possesses a more slowly increasing hardening curve and/or a larger cap aspect ratio. Based on these findings, we suggest that the compressible character of the specimen be taken into account, especially for a powder compact with a slowly increasing hardening curve and/or with a large cap aspect ratio; the current cross sectional area of the specimen needs to be determined by measuring not only the axial strain but also the radial strain of the specimen.

© 2015 Elsevier B.V. All rights reserved.

## 1. Introduction

The computer simulation of compaction behavior of particulate materials (e.g., ceramic, metal, and pharmaceutical powders) has received much interest from the viewpoints of optimizing their processing and of understanding the physics behind the processing [1–5]. In addition to shear yielding (failure) behavior, particulate materials exhibit hydrostatic pressure-dependent yielding behavior, while yielding of bulk metals does not show hydrostatic pressure dependency. In this sense, the Drucker–Prager (DP) constitutive model has been widely used as its yield (shear failure) surface is pressure dependent [6]:

$$f(p, q) = q - p \tan \beta - d = 0 \quad (1)$$

where  $q$  is the Mises equivalent shear stress,  $p$  is the mean stress (pressure),  $\tan \beta$  is the slope of the shear failure surface, and  $d$  is the intercept of the  $q$  axis.  $\beta$  has a physical meaning of the internal friction angle of particles. It is determined by the slope of the shear stress line in the shear stress–pressure domain and reflects the degree of interlocking and surface roughness of the particles.  $d$  is called cohesion which is the shear stress when the applied pressure is zero; it is the cohesive

strength of the particulate material itself when no external pressure is applied.

While the DP model is an elastic–perfectly plastic model, the description of the work hardening phenomenon was achieved in later-developed models by introducing the concept of the cap to the DP model, as seen in the Drucker–Prager cap (DPC) model [7], the modified Drucker–Prager cap (MDPC) model [5,8], the geological cap model [9], and the continuous surface cap model [9,10]. In order to utilize the DP model as well as these advanced cap constitutive models that employ the DP-type shear failure yield surface, the determination of  $d$  and  $\beta$  is a prerequisite. In order to determine these shear failure surface parameters, the conventional triaxial test has traditionally been used, which measures the deviator stress at varying confinement pressures [11–13]. However, for powder compacts such as ceramic green bodies, metal pre-forms, and pharmaceutical tablets, the shear failure surface parameters have been determined very conveniently by employing two simple tests: the unconfined compression (UC) test [14–30] and the diametral test [14–31]. As seen in Fig. 1, the determined failure strengths by the two tests mark two points in the meridional plane, which are used to determine the intercept ( $d$ ) and the slope ( $\tan \beta$ ) of the shear failure surface. In this process, the measured failure strengths from the two tests are assumed to be located on the linear lines with the slopes of 3 and  $3\sqrt{13}/2$ , respectively, in the meridional plane (Fig. 1).

This study focuses on an issue that needs to be clarified in UC testing of a powder compact in order to utilize the UC test as a tool to determine

\* Corresponding authors. Tel.: +82 2 970 6434; fax: +82 2 979 7032.

E-mail addresses: [hshin@gwnu.ac.kr](mailto:hshin@gwnu.ac.kr) (H. Shin), [jbkim@seoultech.ac.kr](mailto:jbkim@seoultech.ac.kr) (J.-B. Kim).

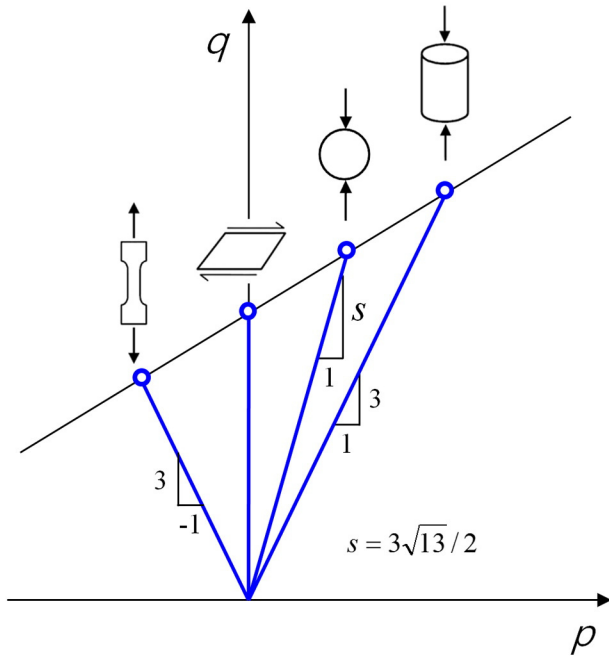


Fig. 1. Schematic illustration for the load paths for various tests.

the shear failure surface of the powder compact. Powder compacts are generally compressible, which is unlike bulk metals where compressibility is negligible. Therefore, in essence, the compressible character of the powder compact has to be accounted for in the process of determining the failure strength in UC testing. However, no such effort has been reported explicitly in the literature for powder compacts [14–30] and for cohesive soils [11,32]. Therefore, here we uncover numerically (by finite element analysis) how much of the measured value of the failure strength based on the assumption of incompressibility of the specimen is different from the value accounting for the compressible character of the specimen. For this purpose, the modified Drucker–Prager cap constitutive model (an elastic–plastic–work hardening model) was employed for a spray-dried  $\text{Al}_2\text{O}_3$  powder compact.

## 2. Numerical analysis

The length-to-diameter ( $L/D$ ) ratio of the specimen considered in this study was 2 (10 mm in diameter and 20 mm in length). The full three dimensional space of the UC test specimen was discretized by eight-node linear brick elements, as seen in Fig. 2. The size of the elements was approximately  $0.83 \times 0.83 \times 2.0 \text{ mm}^3$  and passed a separate mesh quality test. The specimen was loaded axially by controlling the displacement of the nodes at the top surface; the axial movement of the top surface was uniform. However, the axial movement of the nodes at the bottom surface was constrained. The radial movement of the top and bottom surfaces was not constrained; no friction between the specimen and the platens was considered. The specimen was not allowed to rotate during the axial loading by fixing the x-movement of a node located at the radial end of the specimen in the y–z plane. The specimen was not allowed to move in the x–y plane by fixing the movement of the center node at the bottom surface of the specimen in all directions. The reaction forces at the nodes located on the top surface of the specimen were summed and divided by the current cross-sectional area of the specimen to calculate the axial stress. In order to calculate the volume change of the specimen during axial loading, the volume of total elements in the specimen was extracted as a history output. A commercial finite element package Abaqus was used for the numerical analysis.

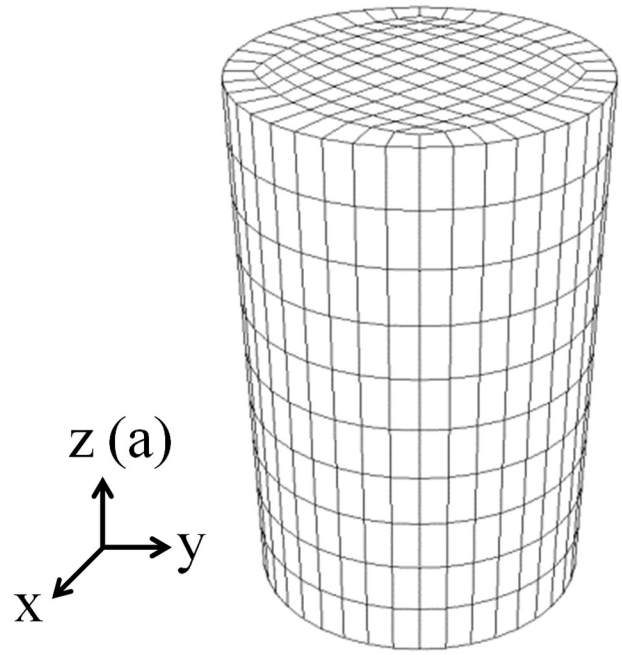


Fig. 2. Geometry and mesh of the model for the specimen with  $L/D = 2$ .

The specimen considered in this study is a spray dried  $\text{Al}_2\text{O}_3$  powder (granules) compact which is widely used in the industry. The modified Drucker–Prager cap (MDPC) model [5,8] implemented in the Abaqus program package was used as the constitutive model. Fig. 3 illustrates the MDPC model schematically. In this figure, the cap is the locus of the iso-volumetric plastic strain points in the meridional ( $q$ – $p$ ) plane; the cap defines the work hardening yield surface. While the DPC model considers a circular cap [7], the MDPC model employs (1) an elliptical cap with aspect ratio  $R$  (Fig. 3) and (2) the transition surface defined by parameter  $\alpha$  (Fig. 3). A detailed description of the employed model (MDPC) is given in our previous study [5]. The working principle of the MDPC model in UC testing is shown in the Appendix (Supplementary material) of this study.

The parameters of the MDPC model were selected in this study by referring to the parameters (properties) for  $\text{Al}_2\text{O}_3$  shown in the literature [33–39] and the selected parameters are shown in parameter set no. 1 (Table 1). In the MDPC model, the relationship between the pressure ( $p$ ) and the inelastic volumetric plastic strain ( $\epsilon_v^{in}$ ) needs to be specified. It controls the movement of the cap (work hardening behavior) of the specimen during loading. In general, the  $p$ – $\epsilon_v^{in}$  relationship (hardening law) of the powder compact varies significantly depending on the type and amount of the binder added to the particles, on the size and shape of the granules formed by the interaction of the particles and the binder, and on the degree of pre-compaction. The same is the case for the spray-dried  $\text{Al}_2\text{O}_3$  as seen in Fig. 4. In this study, the reference  $p$ – $\epsilon_v^{in}$  curve was arbitrarily constructed (curve A in Fig. 4) which is located among various curves for spray-dried  $\text{Al}_2\text{O}_3$  compacts available in the literature.

Another  $p$ – $\epsilon_v^{in}$  curve (curve B) was also constructed in this study by shifting curve A by  $-0.1$  along the abscissa in order to consider a powder compact with a more rapidly increasing hardening curve. In the cap-type constitutive models [5,8–10], the  $p$ – $\epsilon_v^{in}$  relationship and the cap aspect ratio ( $R$ ) control the compressible character of the specimen in the plastic deformation regime (the relationship between  $R$  and the compressible character of the specimen will be discussed in detail later). In order to uncover the behavior of the specimens with different compression characters, systematic variations from the  $p$ – $\epsilon_v^{in}$  relationship and the  $R$  value of the parameter set no. 1 were considered: curve B and a different value of  $R$  (0.25) were also adopted in the numerical analysis as seen in Table 1 (parameter set nos. 2–4).

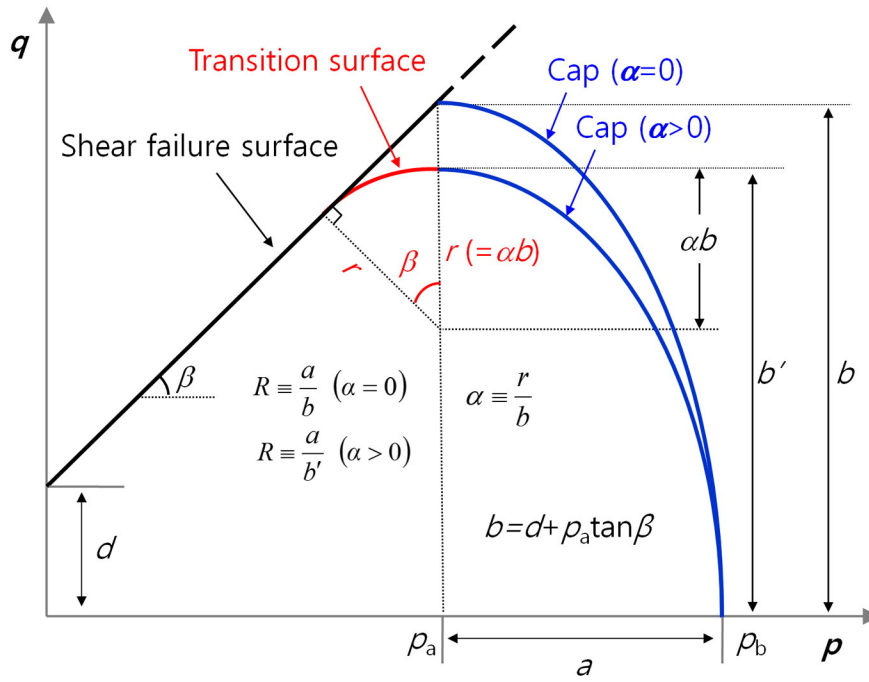


Fig. 3. Employed constitutive model (the modified Drucker–Prager cap model [5]) for the powder compact specimen.

In addition to the material parameters shown in Table 1, two immaterial parameters need to be specified for the numerical calculation using the MDPC model: the transition surface parameter  $\alpha$  and the initial inelastic volumetric strain  $\epsilon_v^{in}(0)$ .  $\alpha$  imposes the computational stability of the MDPC model, which was set to be zero in this study, as no problem was encountered during the numerical analysis.  $\epsilon_v^{in}(0)$  is the initial inelastic volumetric strain of the material when the analysis begins. According to the hardening law (the  $p$ - $\epsilon_v^{in}$  relationship),  $\epsilon_v^{in}(0)$  defines the required pressure to initiate the plastic deformation of the specimen. Thus,  $\epsilon_v^{in}(0)$  describes the degree of pre-compaction of the particulate material when the analysis begins. We set  $\epsilon_v^{in}(0)$  as zero, which means that the required pressure to initiate the plastic deformation of the specimen is the intercept of the pressure axis in Fig. 4; the specimen was assumed to be compacted initially by this pressure value (2.57 MPa and 3.25 MPa for the compact with hardening curves A and B, respectively).

### 3. Results and discussion

#### 3.1. Reference powder compact (parameter set no. 1)

We first consider the reference powder compact with parameter set no. 1 ( $R = 0.5$  and curve A for the  $p$ - $\epsilon_v^{in}$  relationship). For this powder compact, two types of the current cross sectional area of the specimen were determined as seen in Fig. 5(a).  $A_i$  is the current cross-sectional area of the specimen determined by assuming that the specimen is incompressible:

$$A_i = A_o / (1 - \epsilon) \tag{2}$$

Table 1  
Employed material parameters of the MDPC model for the spray dried  $Al_2O_3$  powder.

Parameter set no.	$d$ (MPa)	$\beta$ (degree)	$E$ (GPa)	$\nu$	$R$	$p$ - $\epsilon_v^{in}$ relationship in Fig. 4
1	4	44	10	0.26	0.5	Curve A
2					0.5	Curve B
3					0.25	Curve A
4					0.25	Curve B

where  $A_o$  is the initial cross-sectional area of the specimen and  $\epsilon$  is the axial engineering strain (positive in compression) determined from the axial movement of the node points on the top surface of the specimen (the axial strain of the specimen). In Fig. 5(a),  $A_c$  is the current cross sectional area of the compressible specimen determined by assuming that the specimen remains as a right circular cylinder and by taking into account the volume change (positive in compression) [11]:

$$A_c = \frac{A_o}{(1 - \epsilon)} \left( 1 - \frac{dV}{V_o} \right) \tag{3}$$

where  $V_o$  is the initial volume of the specimen. Note that the incompressibility assumption ( $A_i$ ) significantly overestimates the current cross sectional area of the compressible specimen ( $A_c$ ).

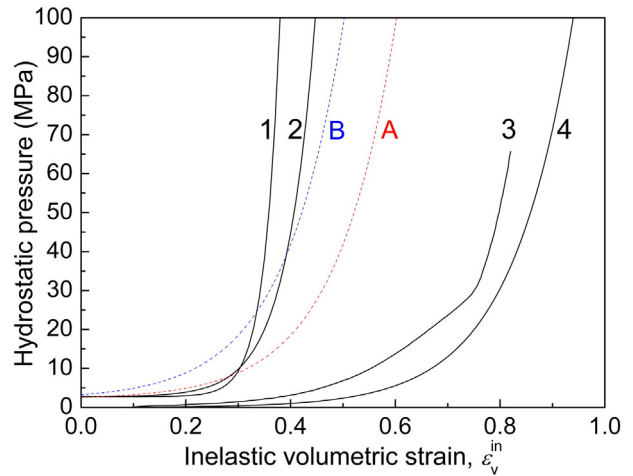


Fig. 4. Pressure vs. inelastic volume strain (hardening) curves for various spray-dried alumina compacts (curve 1: Zeuch et al. (99%.5%  $Al_2O_3$ ) [12], curve 2: Zeuch et al. (94%  $Al_2O_3$ ) [12], curve 3: Riedel and Kraft [33], curve 4: Foo et al. [35]). Curve A was used as the reference hardening curve in this study and curve B was used to investigate the behavior of the specimen with a more rapidly rising hardening curve than the reference curve (curve A).

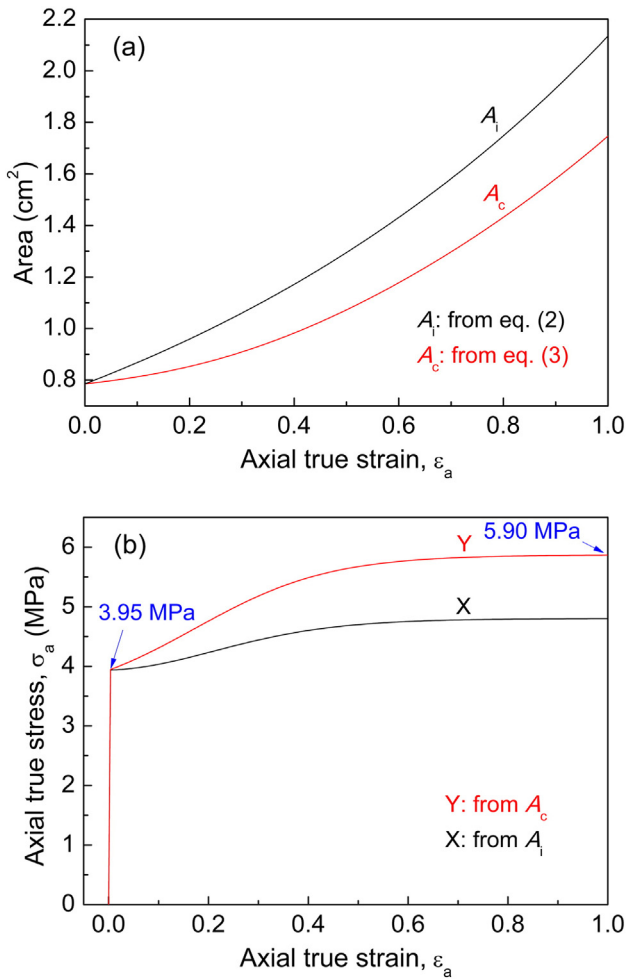


Fig. 5. (a) Current cross sectional areas and (b) axial stress vs. axial strain curves of the powder compact having parameter set no. 1.

Two types of the axial stress of the specimen were determined by dividing the reaction force monitored at the nodes on the top surface of the specimen by  $A_i$  and  $A_c$ , respectively, and the results are shown in Fig. 5(b) as curve X and curve Y. In experiments, the fracture strength is characterized by the stress (maximum in general) followed by its decrease. In some cases, the stress can reach the maximum and stabilize without a fracture (perfect plastic material for example). As explained in the Appendix (Supplementary material), the analytically calculated failure strength of the compressible specimen is 5.9 MPa (the shear failure surface shown in Fig. 1), indicating that the saturated stress state in Fig. 5(b) (marked as Y, 5.9 MPa) is the ultimate failure state.<sup>1</sup> Therefore, in Fig. 5(b), the phenomenon of fracture is considered to occur when the powder compact reaches the ultimate failure state marked as 5.9 MPa. However, in the simulated curves of Fig. 5(b), the abrupt decrease of the stress at a certain strain (the fracture strain), i.e., the phenomenon of fracture, is not captured because the employed MDPC model simply describes the ultimate failure state appearing after work hardening behavior of particulate materials. Such a feature is also the case for other cap-type models such as the geological cap model and the continuous surface cap model. Because the employed model does not describe the phenomenon of fracture, the ultimate failure strength (the value of the saturated axial stress in Fig. 5(b)) was used in this study as a parameter to judge the necessity of considering

<sup>1</sup> The ultimate failure state is the state in which no further change in volume or shear stress occurs.

the compressible character of the specimen in determining the axial stress vs. axial strain plot of the powder compact in UC testing, which is used to determine the fracture strength.

As seen in Fig. 5(b), the (ultimate) failure strength of the compressible compact (curve Y) is much higher than the determined value under the assumption of the incompressible specimen (curve X). The numerically obtained yield strength and the failure strength on curve Y are 3.95 MPa and 5.90 MPa, respectively, which values are consistent with the values determined by the analytical calculation (Supplementary material). Therefore, the numerically determined curve Y reflecting the compressible character of the specimen is the true material property of the specimen. In Fig. 5(b), curve X, based on the assumption of the incompressible specimen, underestimates the actual failure strength of the compressible specimen (curve Y) by 18.2%. This observation occurs because, at a given axial strain, the current cross sectional area determined by the assumption of the incompressible specimen ( $A_i$ ) is larger than the actual area of the compressible powder compact ( $A_c$ ) with reduced volume, as seen in Fig. 5(a).

### 3.2. Powder compact with a more rapidly rising hardening curve (parameter set no. 2)

Now consider the powder compact with a more rapidly increasing hardening curve (curve B and  $R = 0.5$ ; parameter set no. 2) than the reference powder compact (curve A and  $R = 0.5$ ; parameter set no. 1). The simulated axial stress vs. axial strain curves are shown in Fig. 6. As seen in this figure, if the incompressibility assumption is adopted (curve X), the degree of underestimation of the failure strength is now 9.6%, which value is diminished from the case of the reference hardening curve A (Fig. 5(a)). Therefore, if the hardening curve increases more rapidly (like curve B), the degree of underestimation of the failure strength by the incompressibility assumption is less pronounced (the degree of underestimation is magnified for the specimen with a more slowly rising hardening curve).

### 3.3. Powder compact with a smaller $R$ value (parameter set no. 3)

Although the  $R$  value of the spray-dried alumina powder compact was reported to be approximately 0.5 [33–37], the powder compact with a smaller  $R$  value ( $R = 0.25$  and curve A; parameter set no. 3) than the reference powder compact ( $R = 0.5$  and curve A; parameter set no. 1) is now considered to uncover the difference of the two failure strengths when the  $R$  value is different. The simulated axial stress vs. axial strain curves when  $R = 0.25$  (curve A; parameter set no. 3) are shown in Fig. 7. As seen in this figure, the degree of underestimation

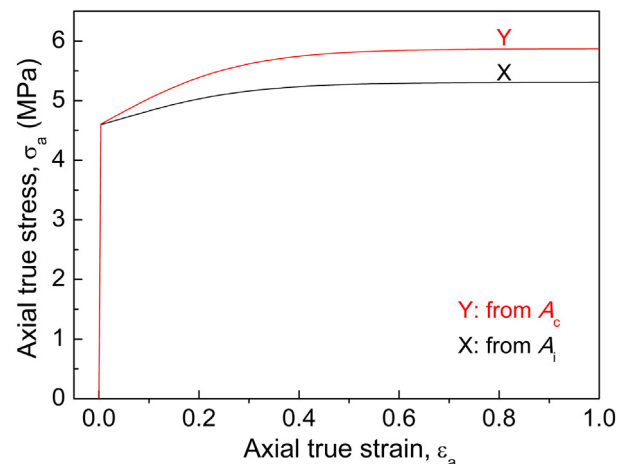


Fig. 6. Axial stress vs. axial strain curves of the powder compact having parameter set no. 2.

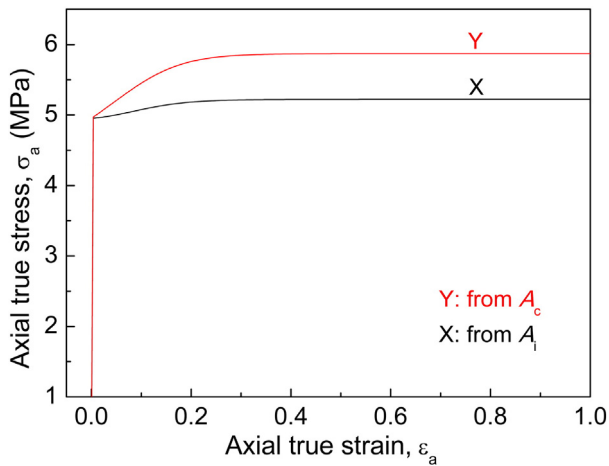


Fig. 7. Axial stress vs. axial strain curves of the powder compact having parameter set no. 3.

of the failure strength is now 11.1%, which value is diminished from the case when the  $R$  value was 0.5 (Fig. 5(a); curve A; parameter set no. 1). Therefore, a decreased  $R$  value decreases the degree of underestimation of the failure strength by the incompressibility assumption (an increased  $R$  value magnifies the degree of underestimation).

We explain why an increased  $R$  value magnifies the degree of underestimation of the failure strength by the incompressibility assumption. For this purpose, refer to Fig. 8 which compares the evolution of the cap surfaces with a large and a small  $R$  values. Assuming that the two caps are initially located at the same position in the hydrostatic pressure axis ( $p_b^*$ ), the load path meets the surface of the large cap earlier at point  $O^L$  than the small cap ( $O^S$ ). Therefore, the powder compact with a large  $R$  value yields at a lower pressure. Now consider the current ( $p, q$ ) state of the specimen during loading. In this current stress state, the cap with a large  $R$  has moved out a longer distance on the hydrostatic axis (to  $p_b^L$ ) than the cap with a small  $R$  has done ( $p_b^S$ ). According to the hardening law, a larger plastic volumetric strain has evolved for the cap with the large  $R$ ; the larger the  $R$  value, the larger the plastic compressibility, which results in a diminished current cross sectional area that leads to the higher failure strength. Therefore, the degree of underestimation of the failure strength by the incompressibility assumption is magnified when the  $R$  value increases. The  $R$  value for a powder compact is determined separately either by the conventional triaxial test [12] or by the confined compression test with the measurements of both the axial and radial stresses [16].

#### 3.4. Powder compact with a more rapidly rising hardening curve and a smaller $R$ value (parameter set no. 4)

Now that the influences of the hardening curve and the  $R$  value on the degree of underestimation of the failure strength by the incompressibility assumption have been uncovered separately, we show that these influences operate additively (independently). For this purpose, the axial stress vs. axial strain curves of the powder compact with parameter set no. 4 ( $R = 0.25$  and curve B) were simulated and the result is shown in Fig. 9. As seen in Fig. 9, the powder compact with a diminished  $R$  value of 0.25 (from the reference value of 0.5) and a more rapidly hardening curve of B (than the reference hardening curve of A) results in a significantly diminished degree of underestimation by the incompressibility assumption (only 1.7%). Thus, the influences of the hardening curve and the  $R$  value on the degree of underestimation of the failure strength by the incompressibility assumption appear additively.

When a powder compact possesses either a rapidly increasing hardening curve or a small  $R$  value, the yield strength increases so that the

difference between the yield strength and the failure strength<sup>2</sup> decreases as seen in the corresponding figures (Figs. 5–7, and 9; see also Table S1 in the Supplementary material). If a powder compact possesses both a rapidly increasing hardening curve and a small  $R$  value, we may ignore the compressible character of the specimen in determining the failure strength by the UC test. Unless a powder compact possesses both such characters, the degree of underestimation by the incompressibility assumption is non-negligible as seen in this and the previous subsections.

#### 3.5. Overall discussion

The elastic modulus and Poisson's ratio ( $\nu$ ) directly control the elastic compressibility of a specimen by the relationship

$$c = 1/K = 3(1-2\nu)/E \quad (4)$$

where  $c$  is the elastic compressibility, and  $K$  is the bulk modulus. In general, the amount of elastic compression of the powder compact specimen is negligible compared to plastic compression, which is controlled by the  $p$ - $\epsilon_v^n$  relationship and  $R$ . Therefore, we cannot simply judge the necessity of accounting for the compressible character of the specimen solely by the term compressibility given in Eq. (4). In the previous subsections, all investigations were carried out under the condition of the same elastic compressibility (constant values of  $E$  and  $\nu$  shown in Table 1).

As seen in the previous subsections, the incompressibility assumption underestimated the failure strength of the powder compact and the degree of underestimation increased when the powder compact possessed a more slowly increasing hardening curve and/or a larger cap aspect ratio. Based on these findings, we suggest that, in the experimental determination of the failure strength of a powder compact, it is generally safe to take the compressible character of the specimen into account. In other words, it is desirable to determine the current area of the deforming powder compact specimen by considering the volume change (compression) of the specimen. For this purpose, the measurement of the radial strain of the specimen is necessary by appropriate means such as the dial gage. When there is friction, the specimen usually barrels during the UC test. In such a case, it is desirable to measure the radial strain at the top (or bottom) and mid height positions at the radial surface. Then, the current cross section areas at the two different positions need to be averaged assuming a linear gradient of the current cross sectional area between the two measurement points. The ASTM standard for the UC testing of soils [32] neglects the compressible character of the specimen: Eq. (2) is used for determining the failure strength of cohesive soils. If a soil compact exhibits a slowly rising hardening behavior and/or a large cap aspect ratio, we suggest that the compressible character of the specimen be accounted for using Eq. (3).

When a heavily over-consolidated compact is subjected to the UC test, after elastic deformation, it may dilate [11,40]. Like other cap-type models, the employed MDPC model is incapable of describing such dilation behavior of the heavily over-consolidated compact. Therefore, curve Y in this study is the compaction behavior of a normally or loosely compacted powder. In this regard, the current study reports the necessity of considering the compressible character of the normally or loosely compacted powder in determining the failure strength by UC testing. The compaction behavior of the normally or loosely compacted powder receives much higher industrial interest than the heavily over-consolidated powder does.

<sup>2</sup> The failure strength (5.90 MPa) is constant regardless of the parameter sets considered in Table 1 because it is determined purely by the shear failure surface as seen in the Supplementary material.

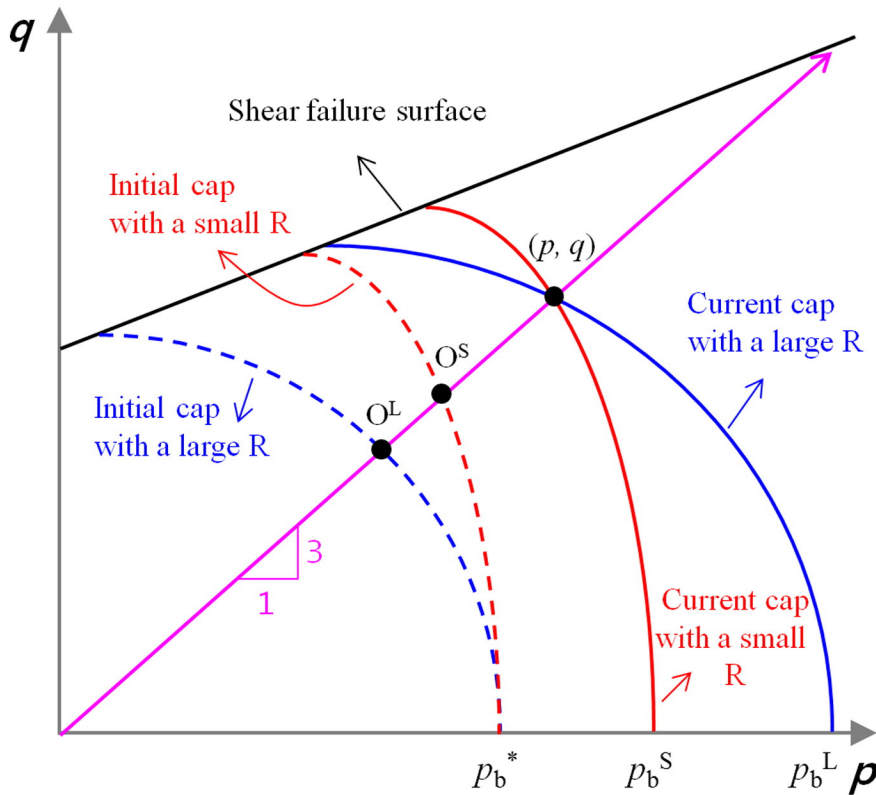


Fig. 8. Schematic illustration for the evolution of the cap surfaces with a large and a small  $R$  values.

4. Conclusion

The effect of the compressible character of a powder compact on the failure strength in unconfined compression (UC) testing is investigated numerically. The modified Drucker–Prager cap constitutive model (an elastic–plastic–work hardening model) was employed for a spray-dried  $Al_2O_3$  powder compact. The ultimate failure strength was used as a parameter to judge the necessity of considering the compressible character of the specimen in determining the axial stress vs. axial strain plot of the powder compact. When the failure strength was obtained from the current cross sectional area determined solely by the axial strain based on the assumption of incompressibility of the specimen, it significantly underestimated the failure strength of the compressible specimen. The degree of underestimation was magnified if the powder

compact possessed a more slowly increasing hardening curve and/or a larger cap aspect ratio. The influences of the hardening curve and the  $R$  value on the degree of underestimation of the failure strength by the incompressibility assumption operated additively. Based on these findings, we suggest that, in the experimental determination of failure strength of the powder compact by UC testing, the compressible character of the specimen be taken into account, especially for a powder compact with a slowly increasing hardening curve and/or with a large cap aspect ratio; the current cross sectional area of the specimen needs to be determined by measuring not only the axial strain but also the radial strain of the specimen.

Supplementary data to this article can be found online at <http://dx.doi.org/10.1016/j.powtec.2015.02.054>.

Acknowledgments

This study was financially supported by the Ministry of Education, Science, and Technology through the National Research Foundation (NRF) of Korea under contract no. 2013R1A1A2007455. The first author (H. Shin) appreciates the technical assistance of Ms. Eun-Hee Jeong at the Industry-Academy Cooperation Foundation, Gangneung-Wonju National University, Republic of Korea.

References

- [1] I. Aydin, B.J. Briscoe, K.Y. Şanhtürk, The internal form of compacted ceramic components: a comparison of a finite element modelling with experiment, *Powder Technol.* 89 (1996) 239–254.
- [2] I. Aydin, B.J. Briscoe, K.Y. Şanhtürk, Dimensional variation of die-pressed ceramic green compacts: comparison of a finite element modelling with experiment, *J. Eur. Ceram. Soc.* 17 (1997) 1201–1212.
- [3] A. Michrafy, D. Ringenbacher, P. Tchoreloff, Modelling the compaction behaviour of powders: application to pharmaceutical powders, *Powder Technol.* 127 (2002) 257–266.
- [4] A. Michrafy, H. Diarra, J.A. Dodds, M. Michrafy, L. Penazzi, Analysis of strain stress state in roller compaction process, *Powder Technol.* 208 (2011) 417–422.

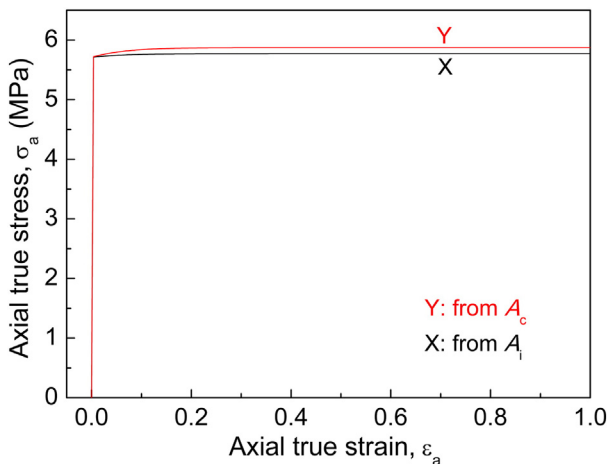


Fig. 9. Axial stress vs. axial strain curves of the powder compact having parameter set no. 4.

- [5] H. Shin, J.-B. Kim, Physical interpretations of cap parameters of the modified Drucker–Prager cap model in relation to the deviator stress curves, *Powder Technol.* (2015) (submitted for publication).
- [6] D.C. Drucker, W. Prager, Soil mechanics and plastic analysis for limit design, *Q. Appl. Math.* 10 (1952) 157–165.
- [7] D.C. Drucker, R.E. Gibson, D.J. Henkel, Soil mechanics and work-hardening theories of plasticity, *Trans. Am. Soc. Civ. Eng.* 112 (1957) 338–346.
- [8] Dassault Systèmes Simulia Corp., ABAQUS Theory Manual 6.132013.
- [9] Livermore Software Technology Corp., LS-DYNA keyword user's manual, *Mater. Models*, vol. II, 2012.
- [10] L.E. Schwer, Y.D. Murray, Continuous surface cap model for geomaterial modeling: a new LS-DYNA material type, 7th Int. LS-DYNA User's Conference, 2009, pp. 16–35–16–50.
- [11] J.P. Bardet, *Experimental Soil Mechanics*, Prentice Hall, Upper Saddle River (NJ), 1997, pp. 443–469 (404–420).
- [12] D.H. Zeuch, J.M. Graziar, J.G. Argüello, K.G. Ewsuk, Mechanical properties and shear failure surfaces for two alumina powders in triaxial compression, *J. Mater. Sci.* 36 (2001) 2911–2924.
- [13] H. Shin, J.-B. Kim, S.-J. Kim, K.Y. Rhee, A simulation-based determination of cap parameters of the modified Drucker–Prager cap model by considering specimen barreling during conventional triaxial testing, *Comput. Mater. Sci.* 100 (2015) 31–38.
- [14] P. Doremus, F. Toussaint, O. Alvain, Simple tests and standard procedure for the characterisation of green compacted powder, in: A. Zavaliangos, A. Laptev (Eds.), *Recent Developments in Computer Modeling of Powder Metallurgy Processes*, IOS Press, 2001, pp. 29–41.
- [15] P. Doremus, Model input data – failure, in: P.R. Brewin, O. Coube, P. Doremus, J.H. Tweed (Eds.), *Modelling of Powder Die Compaction*, Springer-Verlag, London Limited, 2008, pp. 95–103.
- [16] J.C. Cunningham, I.C. Sinka, A. Zavaliangos, Analysis of tablet compaction. I. Characterization of mechanical behavior of powder and powder/tooling friction, *J. Pharm. Sci.* 93 (8) (2004) 2022–2039.
- [17] C. Lu, Determination of Cap Model Parameters Using Numerical Optimization Method for Powder Compaction Ph.D. Thesis Marquette University, 2009.
- [18] Y.-B. Kim, J. Lee, S. Lee, H.-J. Park, G.-A. Lee, Calibration of a density-dependent modified Drucker–Prager cap model for AZO powder, *Adv. Mater. Res.* 482–484 (2012) 1249–1256.
- [19] J. Lee, Y.-B. Kim, S. Lee, J.-H. Song, J.-S. Park, G.-A. Lee, A density-dependent modified Drucker–Prager cap model of indium tin oxide powder, *Adv. Sci. Lett.* 15 (2012) 281–284.
- [20] I.C. Sinka, J.C. Cunningham, A. Zavaliangos, The effect of wall friction in the compaction of pharmaceutical tablets with curved faces: a validation study of the Drucker–Prager cap model, *Powder Technol.* 133 (2003) 33–44.
- [21] O. Coube, H. Riedel, Numerical simulation of metal powder die compaction with special consideration of cracking, *Powder Metall.* 43 (2000) 123–131.
- [22] H. Diarra, V. Mazel, V. Busignies, P. Tchoreloff, FEM simulation of the die compaction of pharmaceutical products: influence of visco-elastic phenomena and comparison with experiments, *Int. J. Pharm.* 453 (2013) 389–394.
- [23] H. Diarra, V. Mazel, A. Boillon, L. Rehault, V. Busignies, S. Bureau, P. Tchoreloff, Finite Element Method (FEM) modeling of the powder compaction of cosmetic products: comparison between simulated and experimental results, *Powder Technol.* 224 (2012) 233–240.
- [24] L.H. Han, J. Elliott, S. Best, R. Cameron, A.C. Bentham, A. Mills, G.E. Amidon, B.C. Hancock, Numerical simulation on pharmaceutical powder compaction, *Mater. Sci. Forum* 575–578 (2008) 560–565.
- [25] C. Shang, I.C. Sinka, J. Pan, Constitutive model calibration for powder compaction using instrumented die testing, *Exp. Mech.* 52 (2012) 903–916.
- [26] F. Podzeck, Investigations into the mechanical strength anisotropy of Sorbitol Instant compacts made by uniaxial compression, *Adv. Powder Technol.* 18 (2007) 361–379.
- [27] D. Souriou, P. Goeuriot, O. Bonnefoy, G. Thomas, F. Dore, Influence of the formulation of an alumina powder on compaction, *Powder Technol.* 190 (2009) 152–159.
- [28] M.C. Leaper, V. Leach, P.M. Taylor, D.C. Prime, A comparison of compacting and caking behaviour of carbonate-based washing powders, *Dry. Technol.* 31 (2013) 769–774.
- [29] V. Mazel, H. Diarra, V. Busignies, P. Tchoreloff, Comparison of the different failure tests for pharmaceutical tablets: applicability of the Drucker–Prager failure criterion, *J. Pharm. Sci.* 470 (2014) 63–69.
- [30] J.T. Fell, J.M. Newton, Determination of tablet strength by the diametral compression test, *J. Pharm. Sci.* 39 (1970) 688–691.
- [31] P. Jonsén, H.-Å. Häggblad, K. Sommer, Tensile strength and fracture energy of pressed metal powder by diametral compression test, *Powder Technol.* 176 (2007) 148–155.
- [32] American Society for Testing Materials, Standard test method for unconfined compressive strength of cohesive soil, ASTM D2166/D2166M, ASTM International, West Conshohocken, PA, 2013.
- [33] H. Riedel, T. Kraft, Chapter 26: Simulation in Powder Technology, *Continuum Scale Simulation of Engineering Materials: Fundamentals – Microstructures – Process Applications*, in: Dierk Raabe, Franz Roters, Frederic Barlat, Long-Qing Chen (Eds.), Wiley-VCH Verlag GmbH & Co., KGaA, 2004.
- [34] T. Kraft, H. Riedel, O. Rosenfelder, Compaction and sintering of a ceramic seal: modeling and experimental response, *Int. J. Powder Metall.* 39 (2003) 27–34.
- [35] Y.Y. Foo, Y. Sheng, B.J. Briscoe, An experimental and numerical study of the compaction of alumina agglomerates, *Int. J. Solids Struct.* 41 (2004) 5929–5943.
- [36] H. Zipse, Finite-element simulation of the die pressing and sintering of a ceramic component, *J. Eur. Ceram. Soc.* 17 (1997) 1707–1713.
- [37] O.G. Abdullah, F.A. Rasin, T.A. Al-Dhahir, Finite element simulation of alumina ceramic powder compaction, *Int. J. Pure Appl. Phys.* 5 (2009) 15–31.
- [38] B.J. Briscoe, N. Özkan, Compaction behaviour of agglomerated alumina powders, *Powder Technol.* 90 (1997) 195–203.
- [39] O. Cazacu, J. Jiu, N.D. Cristescu, A new constitutive model for alumina powder compaction, *KONA 1997 (1997)* 103–112.
- [40] W.-F. Chen, *Constitutive Equations for Engineering Materials*, vol. 2, Elsevier, New York, 1994, pp. 1002–1008.

## Supplementary data (Appendix)

### Analytical calculations for the compressible specimens

Consider the reference powder compact with parameter set No. 1 with curve A (Table 1 in the main text). For hardening curve A, the intercept of the ordinate in the  $p$ - $\varepsilon_v^{\text{in}}$  plane is 2.57 MPa ( $p_b$ ) as indicated in Fig. S1. Since the initial inelastic volumetric strain  $\varepsilon_v^{\text{in}}(0)$  is set to zero, a hydrostatic pressure of 2.57 MPa is required to initiate the plastic deformation; the specimen is assumed to be initially compacted by this hydrostatic pressure. Therefore, in the  $q$ - $p$  plane (Fig. S2), the cap is initially positioned at  $p_b$  (2.57 MPa) in the hydrostatic pressure axis.

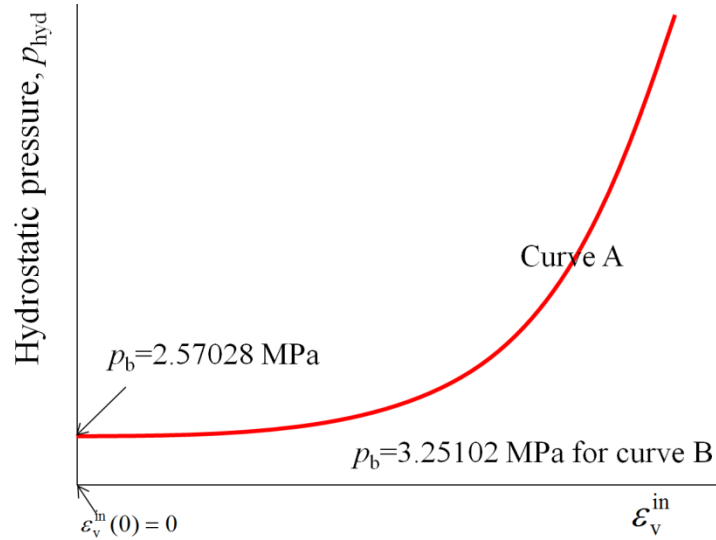


**Fig. S1.** Hardening curve A in parameter set No. 1.

In Fig. S2, the values of  $b$ ,  $a$ , and  $p_a$  are determined as follows. By inserting point  $(p_a, b)$  into the equation of the shear failure surface ( $q = d + p \tan \beta$ ),

$$b = d + p_a \tan \beta \quad (\text{A1})$$

From the definition of  $R$  ( $R \equiv a/b$ ),

$$p_b - p_a = Rb \quad (\text{A2})$$

By solving equations (A1) and (A2), we get  $b=4.37$  MPa,  $a=2.19$  MPa, and  $p_a=0.38$  MPa.

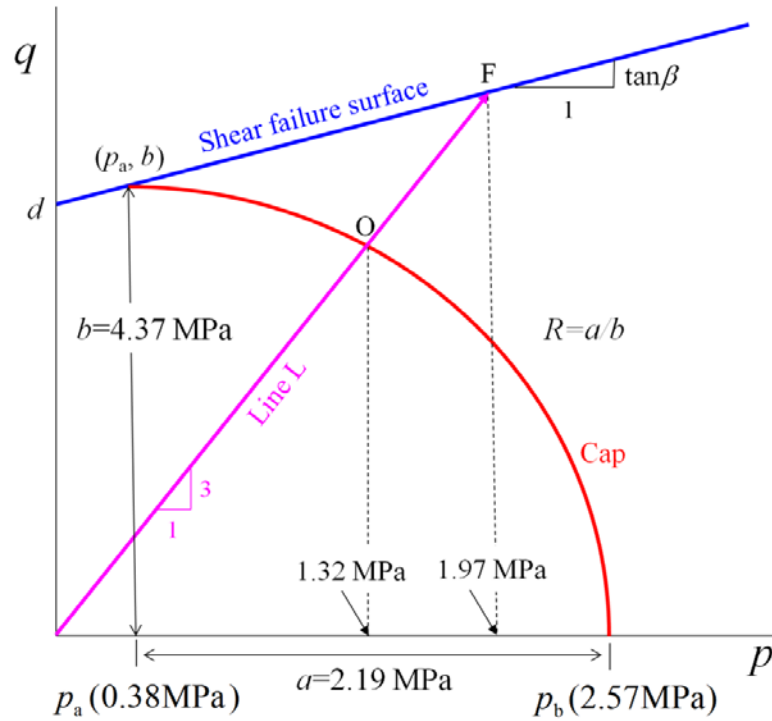


**Fig. S2.** Working principle of the MDPC model for UC testing (Parameter set No. 1). The illustrated cap is located at its initial position.

In UC testing, the stress state of the specimen progresses along line L (with a slope of 3) in the  $q$ - $p$  plane. When the current stress state of the specimen is located inside the region surrounded by the cap, the specimen deforms elastically. The specimen yields when the stress

state reaches the cap (point O) at which the current pressure of the specimen is 1.32 MPa. This value (1.32 MPa) is obtained by considering the intersection between line L (equation A3) and the cap when  $\alpha=0$  (equation A4):

$$q = 3p \quad (\text{A3})$$

$$(p - p_a)^2 + R^2 q^2 = R^2 b^2 \quad (\text{A4})$$

By solving equations (A3) and (A4), we get  $p=1.32$  MPa, which is the pressure of the specimen at the moment of yielding. This pressure value corresponds to the axial stress value of 3.95 MPa by the relation  $p=(\sigma_x+\sigma_y+\sigma_z)=\sigma_z/3=\sigma_a/3$  ( $\sigma_x=\sigma_y=0$ ) which value is consistent with the numerically determined value (3.95 MPa) as marked in Fig. 5(b).

Although a pure hydrostatic loading requires the pressure of 2.57 MPa to initiate the plastic deformation ( $\varepsilon_v^{\text{in}}=0$ ), in UC testing which follows load path L (Fig. S2), the specimen deforms plastically at the pressure value of only 1.32 MPa ( $\varepsilon_v^{\text{in}}=0$ ). Note that the current plastic volumetric strain at point O (in UC testing) is the same as that at point  $p_b$  (in hydrostatic compression testing): the cap is the locus of the iso-plastic-volumetric strain points.

When the current stress state of the specimen moves out from the surface of the initial cap with the onset of the plastic strain ( $\varepsilon_v^{\text{in}}=0$ ) and work hardening thereafter ( $\varepsilon_v^{\text{in}}>0$ ), a new cap surface is defined at each stress state so that the current stress state of the specimen ( $p, q$ ) is always on the cap surface. In order to define the new cap surface, the position of the cap

shifts on the hydrostatic axis from the value of 2.57 MPa and the shifted location is determined by the hardening curve (Fig. S1), which increases from the value of 2.57 MPa as the inelastic (plastic) volumetric strain increases from zero.

The movement of the cap (work hardening) ends when the stress state reaches the shear failure surface (ultimate failure state). The pressure at the intersection point (F) between line L and the shear failure surface can be obtained by solving the failure surface equation ( $q=d+p\tan\beta$ ) and equation (A3). In this way, we get  $p=1.97$  MPa. This pressure value corresponds to the axial stress value of 5.90 MPa by the relation  $p=\sigma_a/3$  which value is consistent with the numerically determined value (5.90 MPa) as marked in Fig. 5(a).

The analytically calculated results shown above are summarized in Table S1 with the cases for other parameter sets. The values of the axial yield strength and the axial ultimate failure strength are consistent with the numerical results in the corresponding figures (Figs. 5-7 and 9; curve Y) in the main text.

**Table S1.** Analytically calculated results for the investigated parameter sets. The unit of  $p_b$ ,  $p_a$ , and the strength is MPa.

Parameter set	No.1	No.2	No.3	No.4
$R$	0.5	0.5	0.25	0.25
Hardening curve	A	B	A	B
$p_b$ (Initial cap)	2.57	3.25	2.57	3.25
$p_a$ (Initial cap)	0.38	0.84	1.26	1.81
$p_b$ (Final cap)	4.92	4.92	3.44	3.44
$p_a$ (Final cap)	1.97	1.97	1.97	1.97
Axial yield strength	3.95	4.61	4.98	5.74
Axial ultimate failure strength	5.90	5.90	5.90	5.90